Bull. Mater. Sci. (2025)48:20
https://doi.org/10.1007/s12034-024-03376-0

Tuning the structural, magnetic and optical properties of $EuCrO_3$ orthochromites through Dy^{3+} substitution

MEENAKSHI[1,†], R KAPOOR[2,3], S DASH[4], R BANSAL[1], A VIJ[1], H K CHOURASIYA[5], N KUMAR[2], RAMOVATAR[1,*] and S KUMAR[2,6,†]

[1]Department of Physics and Astrophysics, Central University of Haryana, Mahendergarh 123031, India
[2]Department of Physics, Sri Venkateswara College, University of Delhi, New Delhi 110021, India
[3]Department of Physics, Brock University, St. Catharines L2S 3A1, Canada
[4]Department of Science & Humanities, MLR Institute of Technology, Hyderabad 500043, India
[5]Material Science Division, Inter University Accelerator Centre, New Delhi 110067, India
[6]Department of Physics, Shivaji College, University of Delhi, New Delhi 110027, India
*Author for correspondence (ramovatar@cuh.ac.in)
[†]These authors contributed equally to this work.

MS received 23 June 2024; accepted 3 November 2024

Abstract. In this study, $EuCrO_3$ (ECO) and $Eu_{0.9}Dy_{0.10}CrO_3$ (EDCO) rare-earth orthochromite compositions were synthesized through the traditional solid-state reaction technique. A comprehensive investigation was conducted to analyse the effect of the substitution of 10 wt% Dy^{3+} ions on the structural, optical and magnetic properties of $EuCrO_3$. The X-ray diffraction results along with Rietveld refinement confirm the monophasic nature with an orthorhombic distorted perovskite structure for both compositions. Field emission scanning electron microscopy reveals polycrystalline microstructures with average grain sizes ranging from 269 to 327 nm for both compounds. The optical bandgap is evaluated by Tauc's relation and is observed to slightly increase from 2.24 to 2.33 eV with Dy^{3+} ions substitution. Optical parameters, including skin depth, extinction coefficient, refractive index and optical conductivity are determined and their variations with Dy substitution are analysed. Temperature-dependent magnetic analysis reveals a Néel temperature (T_N) of 177 K in EDCO composition, lower than that of pristine $EuCrO_3$ ($T_N \sim 181$ K). The magnetocaloric effect of the EDCO compound demonstrates a magnetic entropy change (ΔS) and relative cooling power of –0.27 J kg^{-1} K and 4.4 J kg^{-1}, respectively, near T_N under the application of 7 Tesla field. This study highlights the tunability of $EuCrO_3$ properties through Dy ion substitution for customized applications.

Keywords. Orthochromites; optical properties; UV/Vis spectroscopy; magnetocaloric effect.

1. Introduction

Rare-earth perovskite oxides have emerged as a noteworthy group of materials that have attracted considerable interest in diverse applications. This is mostly due to their extensive and captivating characteristics, particularly their magnetic, electrical and photocatalytic capabilities [1–5]. Rare-earth orthochromites (a subgroup of perovskite oxides) with a general formula $RCrO_3$ (where R is trivalent rare-earth metal ions) are showing a significant interest due to their magnetic properties [6–8]. These materials exhibit different kinds of magnetic interactions, such as R^{+3}–R^{+3}, Cr^{+3}–Cr^{+3} and Cr^{+3}–R^{+3} interactions. These interactions have a substantial impact on the determination of several magnetic properties, including magnetization reversal [9], spin reorientation [10], exchange bias [11] and magnetocaloric effect [12,13]. Such properties have made orthochromites the potential applicants for sensors thermally assisted random access memory, thermomagnetic switches and magnetic refrigeration [11,14]. Generally, orthochromites exhibit deformed perovskite structures along with *Pnma* space group symmetry and below their Neel temperature (T_N), they often exhibit canted antiferromagnetic arrangement in the G-type configuration. This phenomenon arises as a result of the antisymmetric Dzyaloshinsky–Moriya interaction [15]. In general, when ionic radii of rare-earth elements reduce from La to Lu, the transition temperature (T_N) of orthochromites shows a monotonically decreasing trend across 282 to 112 K [16].

In recent years, researchers have been increasingly drawn to the semiconducting behaviours exhibited by rare-earth-based orthochromites, driven by their potential applications in optoelectronic devices like photodetectors, light-emitting diodes and photocatalytic activities [2,17,18]. The exciting

Published online: 11 January 2025

optical properties of rare-earth-based perovskites arise due to intra-band transitions in the 4f orbital. Due to their optical absorption, emission properties and long luminous lifetime, these materials are widely useful for the making of optical devices. Numerous studies in the past few years have delved into the optical properties of orthochromites. Gupta and Poddar [19] determined an optical bandgap of approximately 2.8 eV for $DyCrO_3$ using optical absorption data, positioning it as a promising candidate for the investigation of photocatalytic activities. Mguedla *et al* [20] explored various optical parameters, including the optical extinction coefficient, refractive index, skin depth, optical conductivity and dispersion energy in $PrCrO_3$ and $HoCrO_3$ compounds [18,20]. The optical properties of orthochromites have also been subject to modulation through the introduction of different transition metals at the Cr site. For instance, Kanwar *et al* [21] observed a decrease in the optical bandgap from 3.22 to 2.01 eV in the $HoCrO_3$ compound after substituting Mn ions, showcasing the tunability of optical properties through doping [22]. Yadav and Rath [23] investigated the optical properties of Fe-modified $CeCrO_3$ compounds.

Researchers have actively explored various materials to assess their potential as low-temperature refrigerants, focusing on the quantification of magnetic entropy change (ΔS) and assessing their relative cooling power (RCP). Orthochromites, in particular, demonstrated encouraging properties for magnetic refrigeration at lower temperatures. Numerous orthochromites including $DyCrO_3$ [23], $GdCrO_3$ [11,24], $SmCrO_3$ [25], $NdCrO_3$ [6] and $LaCrO_3$ [26], among others, have undergone comprehensive investigations with reported results on their magnetic properties. The objective of these investigations is to assess their applicability and effectiveness for use in magnetic refrigeration. For instance, Kumar *et al* [9] reported a $-\Delta S$ value of approximately 3.788 J kg^{-1} K^{-1} under a 90 kOe field with a 215.22 J kg^{-1} relative cooling power in manganese-modified $EuCrO_3$ orthochromites. Yin and Jain [27,28] demonstrated enhanced magnetocaloric properties with an increase in the doping content of Gd in $HoCrO_3$. They also explored the particle size dependence on the magnetocaloric properties of $HoCrO_3$ [28]. Shi *et al* [13] conducted a comparative study, reporting a maximum $-\Delta S$ value of $\sim$27.6 J kg^{-1} K^{-1} at 5 K and 7 T with a relative cooling power of $\sim$531.1 J kg^{-1}, through Gd substitution in $ErCrO_3$ at the R-site [13]. Panwar *et al* [22] developed Mn-substituted $Gd_{0.5}Er_{0.5}CrO_3$ orthochromites with a $-\Delta S$ value of 16.78 J kg^{-1} K^{-1} and a relative cooling power of 375.941 J kg^{-1} at 5 T [29]. Among all orthochromites, $EuCrO_3$ stands out as orthorhombic G-type antiferromagnetic (AFM) along the transition temperature near 181 K [30,31].

The primary aim of this research is to explore the effects of Dy^{3+} ions doping on the structural, morphological, optical and magnetic properties of the $EuCrO_3$ compound. The motivation for doping with Dy^{3+} ions lies in their larger magnetic moment (10.63 μ_B) compared to the non-magnetic Eu^{3+} ions (0 μ_B). Substituting Dy^{3+} is expected to enhance the magnetic properties of the ECO compound by altering the magnetic interactions within the Cr^{3+} sublattice. This could lead to improved magnetic ordering or the emergence of new magnetic phases, broadening the material's potential applications. As far as we are aware, this is the first-ever study on such a detailed investigation of the physical properties of $EuCrO_3$ compounds. With significant optical and magnetic properties, Dy^{3+}-doped $EuCrO_3$ compounds can be promising candidates for various potential applications.

2. Experimental

Polycrystalline $EuCrO_3$ (ECO) and $Eu_{0.9}Dy_{0.10}CrO_3$ (EDCO) samples were synthesized via the traditional solid-state reaction process. High-purity powders of Eu_2O_3 (99.90%) and Cr_2O_3 (99.90%) were employed in stoichiometric proportions as precursors. The raw materials underwent meticulous mixing in an agate mortar and ground continuously for 4 h to ensure homogeneity. Subsequently, the obtained powders underwent a two-step calcination process. Initially, the ground powder was heated to 600°C for 24 h. Following this, the calcined powder was further ground for 4 h and subjected to a second calcination at 900°C for 12 h. In the final stage, the powder was compressed into pellets under hydrostatic pressure and sintered in air at 1350°C for 36 h.

Structural analysis of the compounds was conducted using a (Bruker D8 advance EcoPro) X-ray diffractometer (Cu K_λ = 1.540 Å) within the range of $20° \leq 2\theta \leq 80°$ at room temperature. To investigate surface morphology and ensure the chemical purity of the synthesized samples, a field-emission scanning electron microscope (FESEM, Zeiss Gemini SEM 500) combined with energy-dispersive X-ray spectroscopy (EDXS) was employed. Optical absorbance measurements were taken at room temperature using a UV-Vis-NIR spectrophotometer (Agilent Technology Cary 5000) across the 200–2500 nm wavelength range.

For magnetic measurements, a vibrating sample magnetometer integrated with the physical properties measurements system (Dynacool, Quantum Design) was utilized. Magnetization *vs.* temperature (*M–T*) data were recorded in both field cooling (FC) and zero-field cooling (ZFC) modes over the temperature range of 5–300 K, applying the magnetic fields from 500 Oe to 2 kOe. In the ZFC mode, samples were cooled from room temperature to 5 K without the presence of an external magnetic field, and magnetization data were collected during the heating cycle under an applied magnetic field. In the FC mode, samples were cooled to 5 K under the applied magnetic field, and magnetization measurements were taken during the subsequent heating. Additionally, magnetization with field (*M–H*) data

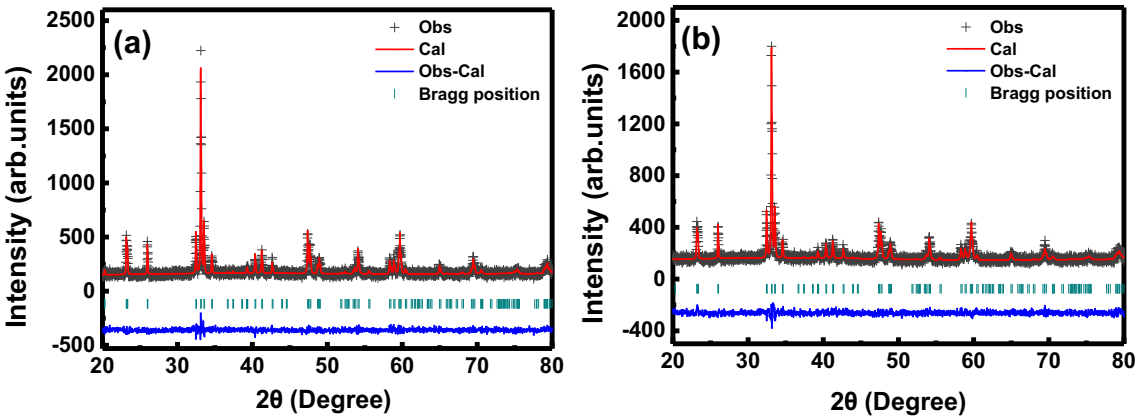

Figure 1. (**a**, **b**) The Rietveld fitted X-ray diffraction spectra of ECO and EDCO compounds at room temperature, respectively.

Table 1. List of obtained structural and microstructural parameters for ECO and EDCO compositions, respectively.

Parameters	ECO	EDCO
a (Å)	5.5117	5.5133
b (Å)	7.6233	7.6220
c (Å)	5.3397	5.3389
V (Å^3)	224.365	224.355
χ^2	1.19	1.17
T	0.869	0.866
S ($\times 10^{-3}$)	31.66	32.20
θ_{101} (°)	14.34	14.45
⟨B–O⟩ (Å)	1.9671	1.9678
$\emptyset_{010}$ (°)	7.863	7.823
R_{avg} (Å)	1.066	1.062
D (nm)	52.46	49.61
G (nm)	269	327

Table 2. List of obtained atomic position from Rietveld refinement for ECO and EDCO compositions, respectively.

Atom	x	Y	Z	Occ.
ECO				
Eu (4c)	0.05409	0.25000	−0.01067	1.052
Cr (4b)	0.00000	0.00000	0.50000	1.060
O1 (4c)	0.47944	0.25000	0.09624	1.301
O2 (8d)	0.218864	0.55121	−0.19583	2.484
EDCO				
Dy (4c)	0.05490	0.25000	−0.00823	0.105
Eu (4c)	0.05490	0.25000	−0.00823	0.900
Cr (4b)	0.00000	0.00000	0.50000	0.996
O1 (4c)	0.47799	0.25000	0.11109	1.205
O2 (8d)	0.29034	1.04399	−0.29004	2.121

were obtained under various temperature ranges (5–300 K) with an applied field of 90 kOe in ZFC mode.

3. Results and discussions

3.1 *Structural analysis*

Figure 1a and b exhibits the Rietveld-fitted XRD patterns of $EuCrO_3$ (ECO) and $Eu_{0.9}Dy_{0.10}CrO_3$ (EDCO) compositions at room temperature. It is clear from the graph that both samples demonstrate a monophasic nature without any secondary phases. The XRD results of pristine composition are analogous to those observed in the previous reports [30–33]. The Rietveld refinement [32] analysis reveals that both compounds possess good agreement with the orthorhombic structure with the *Pnma* space group. Table 1 illustrates the lattice parameters, the unit cell volume, the goodness fitting parameter (χ^2), and the reliability factors of both the samples collected from refinement. It is evident from table 1 that the doping of Dy^{3+} ions at the Eu-site has led to a reduction in the lattice volume. This decrease can be attributed to the lower ionic radii of Dy^{3+} ion (r^{3+}_{Dy} = 1.027 Å) than the Eu^{3+} ion (r^{3+}_{Eu} = 1.066 Å). Atom and Wyckoff's position of the different ions obtained from the refinement is also present in table 2. Goldschmidt tolerance factor (t) calculations, using Cr-O and Eu/Dy-O bond lengths, reveal a value of $t < 1$ for both samples, indicating cooperative rotation of CrO_6 octahedra. Notably, the obtained t-values fall below 1, emphasizing the considerable octahedral distortion.

The orthorhombic strain factor (S), defined as $S = 2(a - c)/(a + c)$ [34], is characterized by the orthorhombic distortion within the unit cell relative to its cubic structure. The corresponding values of the tolerance factor (t) and orthorhombic distortion (S) for ECO and EDCO samples are summarized in table 1. It is noteworthy that the Eu^{3+} ions

have a greater ionic size than the Dy^{3+} ions [7,23], consequently, the value of t is smaller, whereas S is high for EDCO as compared to ECO. To further elucidate the structural changes induced by Dy substitution, the octahedral distortion was evaluated using tilt angles ($\theta_{[101]}$ and $\Phi_{[010]}$) along with the octahedral bond length (R–O) according to the Zhao formalism [35], as expressed by the following equations;

$$\theta_{[101]} = \cos^{-1}(c/a) \quad (1)$$

$$\mathrm{B{-}O} = ab/4c \quad (2)$$

$$\Phi_{[010]} = \cos^{-1}\sqrt{2c}/b \quad (3)$$

The corresponding values are presented in table 1. The results indicate that the octahedral bond angle (R–O) experiences a decrease upon Dy substitution, attributable to the smaller radius of Dy^{3+} ions compared to Eu^{3+} ions. Moreover, the rotational angle $\Phi_{[010]}$ exhibits a decrease, while the tilt angle $\theta_{[101]}$ demonstrates an increase with the incorporation of Dy^{3+} ions on the R-site.

The crystallite size (D) of the samples was calculated by the Scherrer formula according to equation 4 [36]:

$$D = K\lambda/(\beta\cos\theta) \quad (4)$$

where K (0.89) represents the dimensionless shape parameter, λ denotes the X-ray beam's wavelength, β signifies the full-width at half-maxima of the Bragg peak, and θ stands for the Bragg angle. The calculated values of D are also listed in table 1, for ECO and EDCO compounds.

3.2 *FESEM micrograph*

Figure 2a and b presents micrographs depicting the characteristics of ECO and EDCO compounds. Notably, the images reveal a high quality of grain growth, with grains exhibiting a polyhedral shape. The average grain size of the samples was calculated by analysing the grain size distribution histogram using Image J software. The graphical representation as shown in figure 2c and d indicates that the average grain size (G) increases with the substitution of Dy ions. Increases in Dy-content may cause an increase in orthorhombic distortion, which results in the development of stress and mass flow. The energy-dispersive X-ray spectroscopy (EDXS) confirmed the stoichiometric ratios of the constituents of ECO and EDCO compounds, as shown in figure 2e and f.

3.3 *Optical analysis*

3.3a *UV–visible diffuse reflectance spectroscopy:* Diffuse reflectance spectroscopic study was conducted at room temperature within the wavelength range of 200–800 nm to investigate the optical properties of ECO and EDCO compounds. Figure 3a and b displays the absorbance spectra within the UV–Vis regions, which possess multiple bands, indicating the presence of electronic transitions in the samples. The energy bands or states in the rare-earth orthochromites are; filled O^{2-}: 2p band, R^{3+}: 4f band, empty Cr^{3+}: 4s band, partially filled Cr^{3+}: 3d narrow bands and R^{2+}: $4f^{n+1}$ extremely narrow bands [19,37]. The absorption spectra of present compounds show two major peaks along with others that indicate the high- and low-energy bands at ~285 and ~614 nm, respectively. The high-energy band originates from the charge-transfer (CT) from 2p (O^{2-}) to 3d (Cr^{3+}) ions in CrO_6 octahedra and 4f–5d electronic transition ($^4A_2 \rightarrow {}^4T_2$). Conversely, the low-energy band is attributed to the $^4A_2 \rightarrow {}^4T_1$ transition and it can be easily explained by considering octahedral crystal field splitting [38]. Apart from this, other bands were observed that correspond to the *4f–4f* electronic transition between the different energy levels of R^{3+} ions [39].

The optical bandgap (E_g) of both compositions was calculated using the Tauc's relation [40].

$$\alpha h\nu = A(h\nu - E_g)^n, \quad (5)$$

here α represents the optical absorption coefficient, $E = h\nu$ denotes the photon energy, A is the proportionality constant, and n is the nature of the transition. Specifically, n takes on values of 1/2 for a directly allowed, 2 for an indirectly allowed, 3/2 for a directly forbidden and 3 for an indirectly forbidden transitions [41]. In the case of orthochromites, a direct allowed transition was observed, consistent with previous reports [17,20,42]. To determine E_g, a linear fit of $(\alpha h\nu)^2$ *vs.* energy ($h\nu$) was performed, as illustrated in the insets of figure 3a and b. The resulting bandgap values were approximately 2.24 and 2.33 eV for ECO and EDCO, respectively. The reason for the increase in bandgap can be the formation of mid-gap states, as reported in $Y_{1-x}Gd_xCrO_3$ and $Sm_{1-x}Gd_xCr_{0.85}Mn_{0.15}O_3$ series [43,44]. The potential modification of the bandgap of ECO through R-site doping with different rare-earth ions has suggested its promising application in optical devices and photocatalytic applications [1].

In addition, various parameter influences the absorbance of electromagnetic radiation, including roughness of the surface, thickness, extinction coefficient and the refractive nature of the sample. Understanding and optimizing these factors can further enhance the performance of the material as a potential candidate in optical devices.

3.3b *Skin depth and optical extinction coefficient:* The skin depth (δ) of the material quantifies the depth to which electromagnetic waves can penetrate it. In this study, the skin depth has been determined for the investigated samples using absorption coefficient data. The distance at which incident radiation drops to 1/e of its initial value is known as the skin depth (δ) and it can be defined in terms of the absorption coefficient (α) using the following formula [45]:

$$\delta = 1/\alpha \quad (6)$$

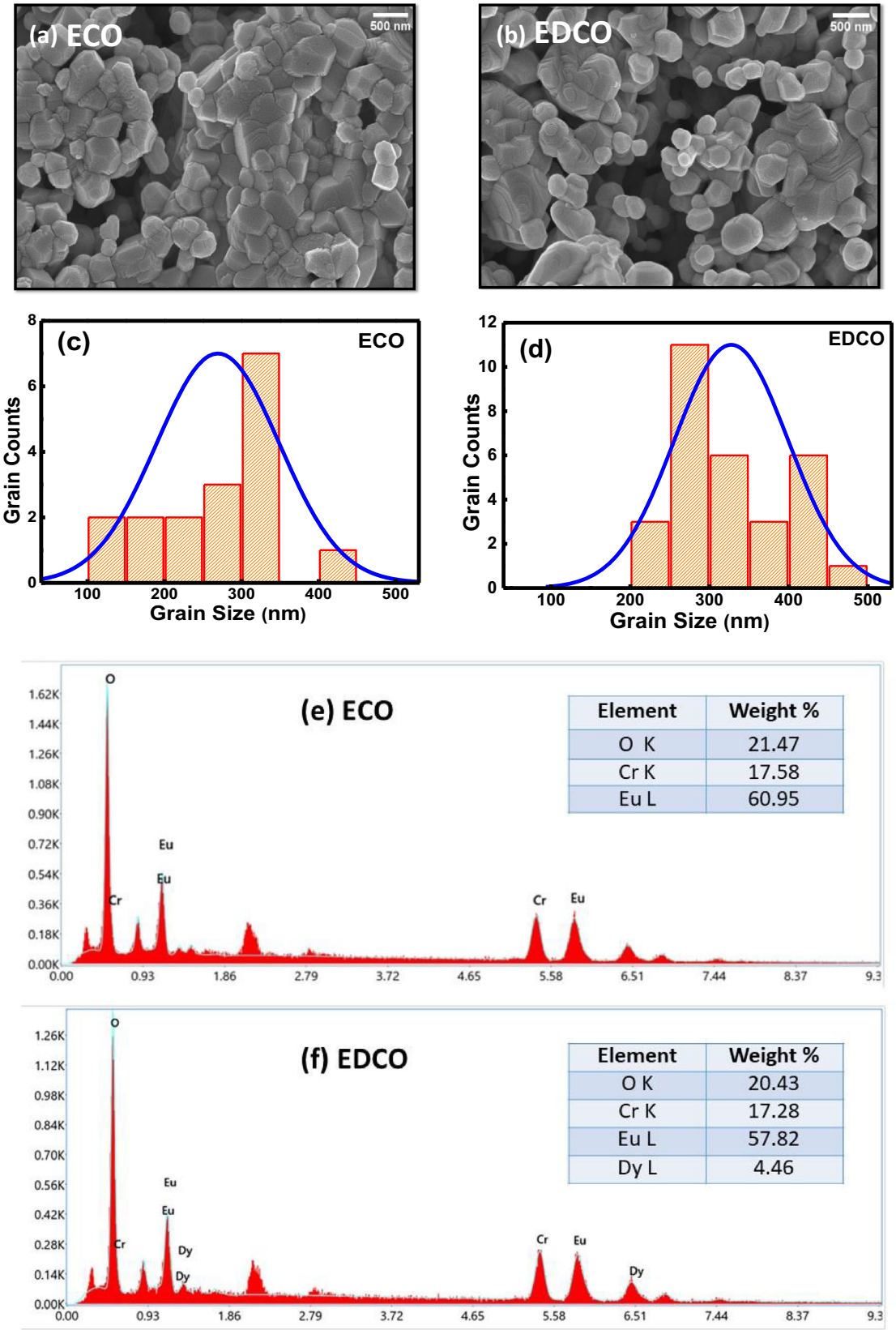

Figure 2. (**a**, **b**) FESEM images, (**c**, **d**) particle size distribution histograms and (**e**, **f**) EDXS images of ECO and EDCO compounds.

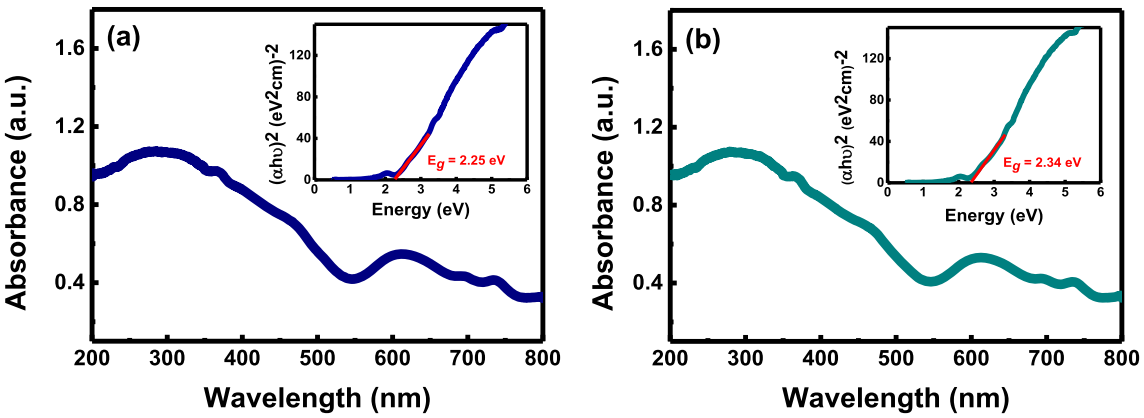

Figure 3. (**a**, **b**) Optical absorption spectra, and insets are the graphs of $(\alpha hv)^2$ *vs.* energy (hv) for the ECO and EDCO compounds.

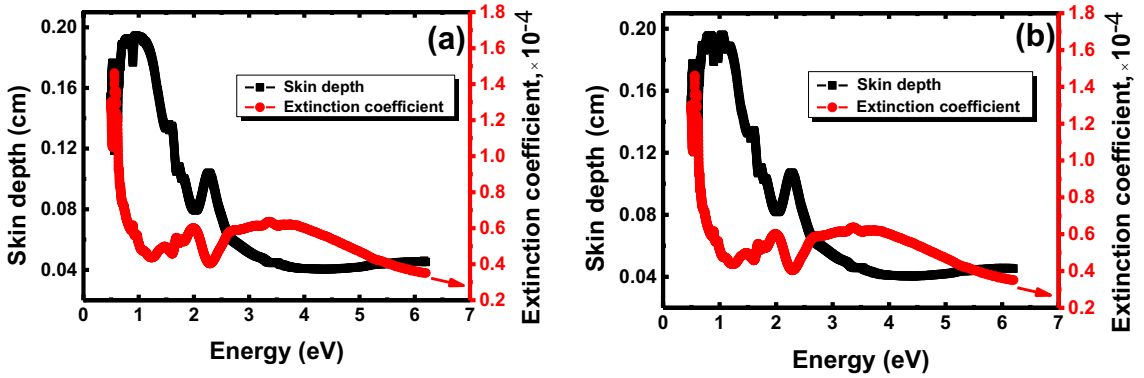

Figure 4. (**a**, **b**) Skin depth and extinction coefficient variation with energy for ECO and EDCO compounds, respectively.

Figure 4a and b depicts the correlation between the incident photon energy (E) and the skin depth (δ) for both compounds. From the figures, it can be inferred that as the incident energy (or frequency) increases, skin depth decreases. At a certain value of energy, the skin depth parameter falls suddenly, and its associated wavelength is known as threshold wavelength (λ_c). Thereafter, skin depth (δ) approaches the minimum value and indicates that penetration becomes more difficult at high frequency. Specifically, the maximum values for the skin depth (δ) in the lower energy range are 0.195 and 0.197 cm for ECO and EDCO compounds, respectively. The values of skin depth proposed that penetration becomes easier in ECO as compared to EDCO.

The extinction coefficient (k) plays a crucial role in characterizing how electromagnetic radiation interacts with a material, encompassing both scattering and absorption phenomena over a given distance within the medium. It is also referred to as the absorption or attenuation index. The extinction coefficient (k) can be calculated using the following expression:

$$k(\lambda) = \alpha\lambda/4\pi \tag{7}$$

here λ represents the wavelength of incident light and $\alpha(\lambda)$ denotes as the absorbance coefficient. In transparent media k-value is nearly zero; however, for absorbing media, it has a significant value. Figure 4a and b shows the variation of extinction coefficient (k) against the incident photon energy (E) for ECO and EDCO compounds. Here, we can notice that the estimated value of the extinction coefficient lies in the range of 10^{-4} to 10^{-5}. This value suggests the transparent nature of the compounds. Upon analysing the data, it is evident that the peak values of k manifest within the lower energy range for both ECO (1.47×10^{-4}) and EDCO (1.48×10^{-4}).

3.3c *Refractive index coefficients:* The most significant optical constant for the material, is the refractive index, indicating how light bends as it traverses through a medium. This property is wavelength-dependent and is influenced by factors such as ionic electronic polarization and the local field within optical materials. Using the following equation, the refractive index (n) can be defined as [46]:

$$n(\lambda) = \frac{1 + R + \sqrt{4R - (1-R)^2[k(\lambda)]^2}}{1 - R} \tag{8}$$

here, the samples' extinction coefficient is denoted by k and the reflectance by R. For the present compounds, k is very small, and equation (8) simplifies in the following form:

$$n(\lambda) = \frac{1 + R^{1/2}}{1 - R^{1/2}} \tag{9}$$

Figure 5a and b depicts the variation of optical refractive index with wavelength. At shorter wavelengths, $n(\lambda)$ exhibits lower values, which subsequently increases with the wavelength, reaching a maximum value of $\sim$8. This phenomenon is explained by the electrons coupling in an oscillating electric field as a result of the resonance effect of incoming electromagnetic radiation and electron polarization. Similar behaviour was also reported in other orthochromites [18,25]. The refractive index values, as illustrated in the inset of figure 5a and b, are noted to range between 3.2 and 4.34 for the visible region. The evolution of the $n(\lambda)$ parameter holds significant importance in the selection of devices for spectral dispersion applications.

3.3d *Dispersion energy and oscillator energy parameters:* The dispersion parameters E_0 and E_d can be calculated by using the following relation, which is proposed by Wemple and Di-Domenico [47]:

$$\frac{1}{n^2 - 1} = \frac{E_0}{E_d} - \frac{(h\nu)^2}{E_d E_0}, \tag{10}$$

where E_0 and E_d denote the single oscillator and dispersion energy, respectively, that calculate the intensity of the inter-band optical transition in the present compounds. Figure 5c and d shows the curve of $(n^2–1)^{-1}$ *vs.* $(h\nu)^2$ by analysing the linear segment of this plot and utilizing equation (10), it is possible to determine parameters E_0 and E_d. The value of (E_0/E_d) is provided by the intercept on the y-axis, while the $1/(E_0/E_d)^{-1}$ value is provided by the slope. E_0 and E_d obtained values are presented in table 3. Notably, E_0 is distinct from the bandgap (E_g), with E_0 found to be ~ 1.9 E_g [48].

Utilizing a similar model, the values of oscillator strength (S_0) and their related oscillator wavelength (λ_0) are also determined by the following relation [49] for both samples.

$$\frac{1}{n^2 - 1} = \frac{1}{S_0 \lambda_0^2} - \frac{1}{S_0 \lambda^2} \tag{11}$$

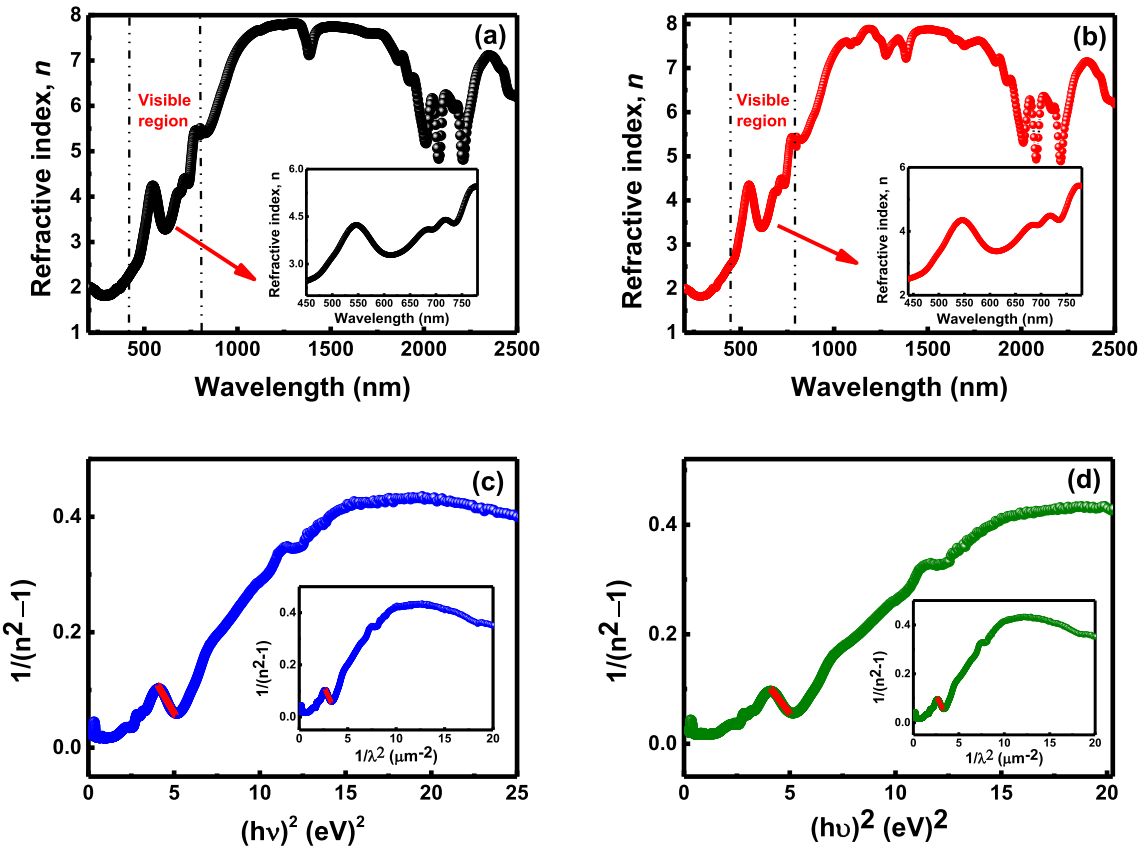

Figure 5. (**a**, **b**) The refractive index variation as a function of wavelength for ECO and EDCO compounds, (**c**, **d**) plot of $(1/(n^2 - 1))$ *vs.* $(h\nu)^2$. Insets in images **c** and **d** show the rise of $(1/(n^2 - 1))$ *vs.* λ^{-2} for the ECO and EDCO compounds.

Table 3. The parameters such as single-oscillator energy (E_0), dispersion energy (E_d), oscillator strength (S_0) and the corresponding oscillator wavelength (λ_0) for ECO and EDCO compounds.

Parameters	ECO	EDCO
E_0	2.48 eV	2.47 eV
E_d	7.950 eV	7.951 eV
λ_0	501.95 nm	497.70 nm
S_0	12.12×10^{-6} nm^2	13.88×10^{-6} nm^2

The curve $(n^2–1)^{-1}$ *vs.* (λ^{-2}) is depicted in the insets of figure 5c and d. The calculated values for λ_0 and S_0 by the linear fitting are listed in table 3.

3.3e *Optical conductivity:* The optical conductivity of a material is contingent upon key optical parameters, including the absorption coefficient ($\alpha(\lambda)$), the refractive index ($n(\lambda)$), the extinction coefficient ($k(\lambda)$) and the frequency of the incident energy. It can be determined by the following equation [46]:

$$\sigma_{op}(\lambda) = \frac{\alpha(\lambda)n(\lambda)c}{4\pi k(\lambda)}, \tag{12}$$

where c denotes the velocity of light. Figure 6a and b depicts the behaviour of optical conductivity ($\sigma_{op}(\lambda)$) with wavelength (λ) for ECO and EDCO compounds. The figure illustrates how optical conductivity diminishes with an increase in the incident photon wavelength. This observation is attributed to the electron being excited at a shorter wavelength by photon energy. Conversely, at longer wavelengths, electrons struggle to initiate the hopping motion of charge carriers, resulting in a decrease in optical conductivity. It is noteworthy that the optical conductivity order is determined to be 10^{10} s^{-1}, which is comparable to other perovskite compounds [20,21,25]. This behaviour emphasizes the significance of incident photon wavelength in influencing the optical properties of ECO and EDCO compounds.

3.4 *Magnetic analysis*

To investigate the magnetic characteristic of the EDCO compound, temperature-dependent dc magnetization data was obtained using under zero-field cooling (ZFC) and field cooling (FC) modes, utilizing an applied magnetic field of 500 Oe, 1 kOe, 1.5 kOe and 2 kOe in the temperature range of 5–300 K, as depicted in figure 7a and d. As shown in the inset of figure 7a, the AFM transition (T_N) was identified from the inflection point of the dM_{FC}/dT curve, with an estimated T_N value of 177 K for the EDCO compound under the applied field of 500 Oe. The measured T_N value for $EuCrO_3$ is ~182 K [30,31,50], while for EDCO is ~177 K. The observed difference in T_N is due to the decreasing R_{avg} [7,34]. At high temperatures (above T_N), ZFC and FC curves overlap, displaying very small positive values of magnetization. This characteristic behaviour suggests the paramagnetic nature at higher temperature ranges.

To explore the magnetic properties within the paramagnetic region, a plot of the inverse magnetic susceptibility (χ^{-1}) *vs.* temperature (T) at H = 500 Oe is presented as illustrated in figure 7b. The Curie constant (C) and the Curie–Wiess temperature (θ) are determined in the paramagnetic region using the Curie–Weiss law: $\chi = C / (T - \theta)$. The fitted values for θ and C were determined as –175 K and 5.43 emu-K Oe-mol^{-1}, respectively. The negative θ value signifies the strong AFM exchange interaction [51]. The effective magnetic moment (μ_{eff}^{exp}) was experimentally determined by the following equation:

$$\mu_{eff}^{exp} = \sqrt{\frac{3k_B C}{N}} = \sqrt{8C}, \tag{13}$$

where k_B is the Boltzmann constant and N is the Avogadro number. The estimated value of μ_{eff}^{exp} is determined to be

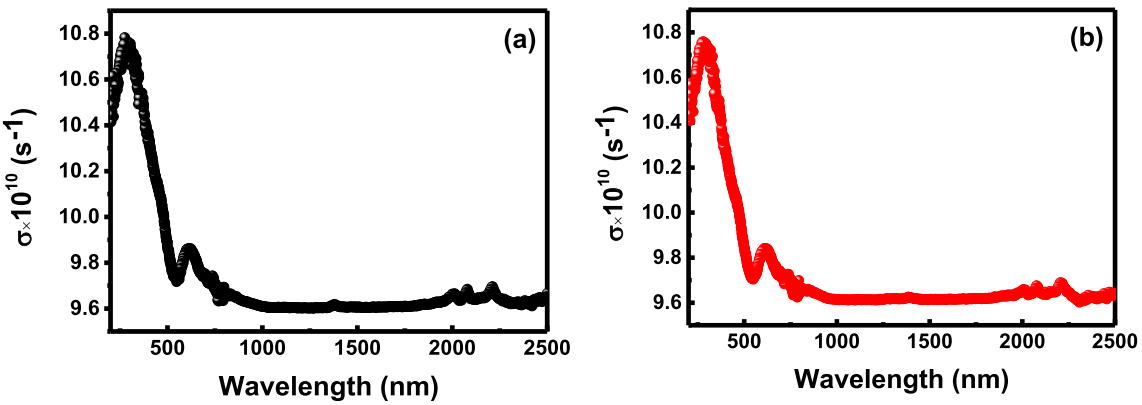

Figure 6. (**a**, **b**) The optical conductivity as a function of wavelength for ECO and EDCO compounds, respectively.

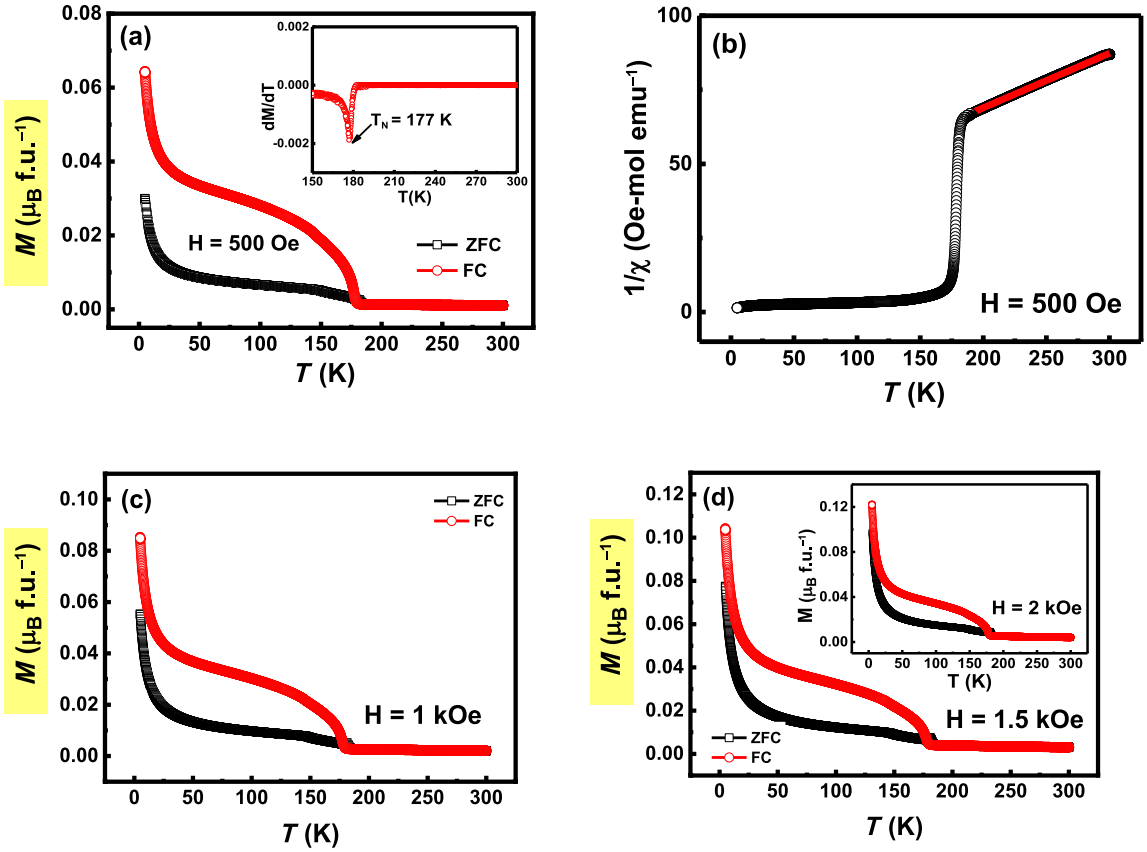

Figure 7. (**a**) ZFC and FC magnetization curves measured at 500 Oe, insets show the first derivative of FC magnetization data. (**b**) Reciprocal of dc magnetic susceptibility χ^{-1} *vs.* temperature at 500 Oe. (**c**, **d**) Magnetization *vs.* temperature plots at 1, 1.5 and 2 kOe.

6.5 μ_B. The theoretical magnetic moment ($\mu_{eff}^{Th.}$) is calculated by the relation:

$$\mu_{eff}^{Th.} = \sqrt{(1-x)(\mu_{eff}^{Eu})^2 + x(\mu_{eff}^{Dy})^2 + (\mu_{eff}^{Cr})^2}$$

where μ_{eff}^{Dy} = 10.63 μ_B, μ_{eff}^{Cr} = 3.87 μ_B and μ_{eff}^{Eu} = 0. The obtained $\mu_{eff}^{Th.}$ value using this calculation is 5.09 μ_B, which is smaller than the experimental value. This discrepancy may arise from the contribution of temperature-dependent Van Vleck paramagnetism of Eu^{3+} ions and its enhancement through the polarization of Eu^{3+} ions by Cr^{3+} ions [9,32].

The FC curve below T_N begins to bifurcate from ZFC due to magnetic irreversibility, leading to a change in the magnetic phase from paramagnetic to AFM with weak ferromagnetism [9]. This phenomenon may arise due to the Dzyoloshinskii–Moriya (DM) antisymmetric exchange interaction [15]. Furthermore, magnetic irreversibility is observed to decrease with an increase in the order of the applied magnetic field (i.e., 1, 1.5 and 2 kOe), as depicted in figure 7c and d. This reduction is probably attributed to the enhancement in the rotation of Cr^{3+} and R^{3+} magnetic ions along the applied field direction.

To better understand the magnetic ordering of the EDCO compound, isothermal magnetization curves were measured as a function of the applied magnetic field in the range of ±9 T at different temperatures (5, 50, 100, 200 and 300 K), as illustrated in figure 8a and b. It is clear from the figure that below T_N, *M–H* loops exhibit symmetrically closed without showing any evidence of saturation within the ±9 T field range. This behaviour is attributed to the simultaneous presence of weak ferromagnetic (FM) components at low field and AFM components at high field. The contribution of the mixed states can be determined by the relation [52]; $M(H) = \chi_{AFM} + M_S$, where the first term (χ_{AFM}) signifies the AFM contribution, and the second term (M_S) represents the magnetization saturation. The M_S value decreases as the temperature increases from 5 K to T_N, indicating an enhanced contribution of weak ferromagnetism at lower temperatures. Above T_N, *M–H* loops disappear, showing a linear increase in magnetization with an applied field which is an indication of the paramagnetic behaviour of the EDCO compound. Additionally, the theoretical value of magnetization saturation (M_S) can be determined using the formula [53]; $M_S = \sum n_i S_i g_i \mu_B$, where n_i is the number of spins of the i-th species, S_i is the spin quantum number of the i-th ion ($S_{Eu3+} = 0$, $S_{Dy3+} = 5/2$ and $S_{Cr3+} = 3/2$) and g_i is the Landé spectroscopic splitting factor ($g_{Eu3+} = 0$ $g_{Dy3+} = 4/3$ and $g_{Cr3+} = 2$) and μ_B is

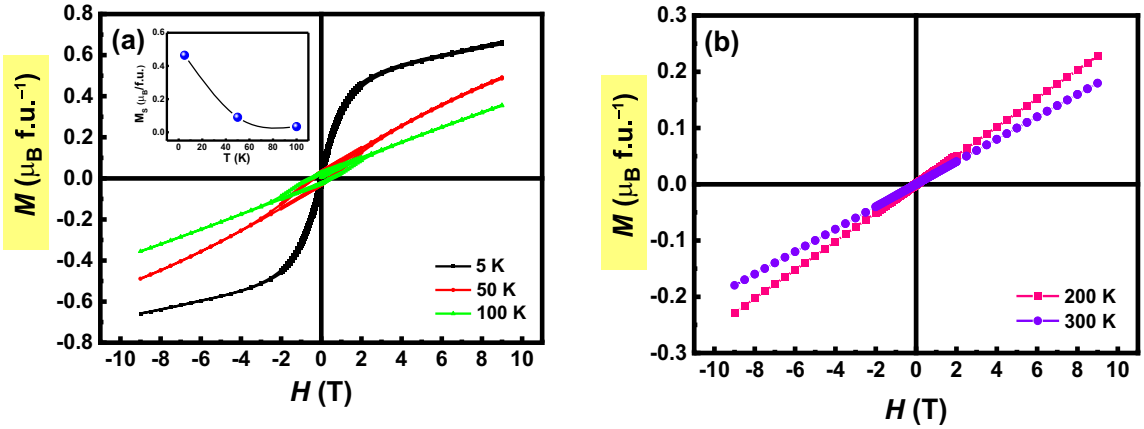

Figure 8. (**a**, **b**) Isothermal magnetization (*M*) *vs.* applied magnetic field (*H*) curve for EDCO at different temperatures between 5 and 300 K under the field of ± 9 T. Inset of (a) shows the magnetization (*M*) *vs.* applied magnetic field (*H*) data at 100 K is subtracted using the linear term χ_{AFH} from *M* to obtain the hysteresis loop of *M* (FM) *vs. H* for EDCO.

the Bohr magneton. By substituting these values in above equation, magnetization saturation is calculated to be ~3.33 μ_B.

The experimental M_S value at 5 K is ~0.46 μ_B f.u.$^{-1}$, which is significantly lower than the theoretical value of ~3.33 μ_B. This discrepancy can be attributed to the strong crystal field effects on Dy^{3+} and the AFM exchange interactions from the Cr^{3+} sublattice [54–56].

3.5 *Magnetocaloric effect*

Isothermal magnetization *vs.* magnetic field (*M–H*) curves were recorded at different temperatures ranging from 160 to 200 K within the field range of 0–9 T, as illustrated in figure 9a. In this study, the magnetocaloric properties were examined by the magnetic entropy change and cooling power with the variation of the external magnetic field. The magnetic entropy change (ΔS) can be determined using the following relations [57,58];

$$\Delta S(T_{av})_{\Delta H} = \frac{\delta H}{2\delta T}\left(\delta M_1 + 2\sum_{i=2}^{n-1}\delta M_i + \delta M_n\right), \qquad (14)$$

here, the average temperature T_{av} is calculated as $((T_j + T_{j+1})/2)$, based on two magnetization isotherms acquired at temperatures T_j and T_{j+1}. These measurements are taken in a magnetic field that changes by an amount ΔH, where $\Delta H = H_F - H_I$ and δH is the constant step size. Here, $\delta T = T_{j+1}$, T_j represents the temperature difference between the two isotherms. For each of the two isotherms, *n* points are measured as the magnetic field varies from $H_1 = H_I$ to $H_n = H_F$ at a step size of $\delta H = \Delta H/(n-1)$. Additionally, $\delta M_i = [M(T_{j+1})_I - M(T_j)_i]$ represents the difference in magnetization between T_j and T_{j+1} for each magnetic field step, ranging from 1 to *n*.

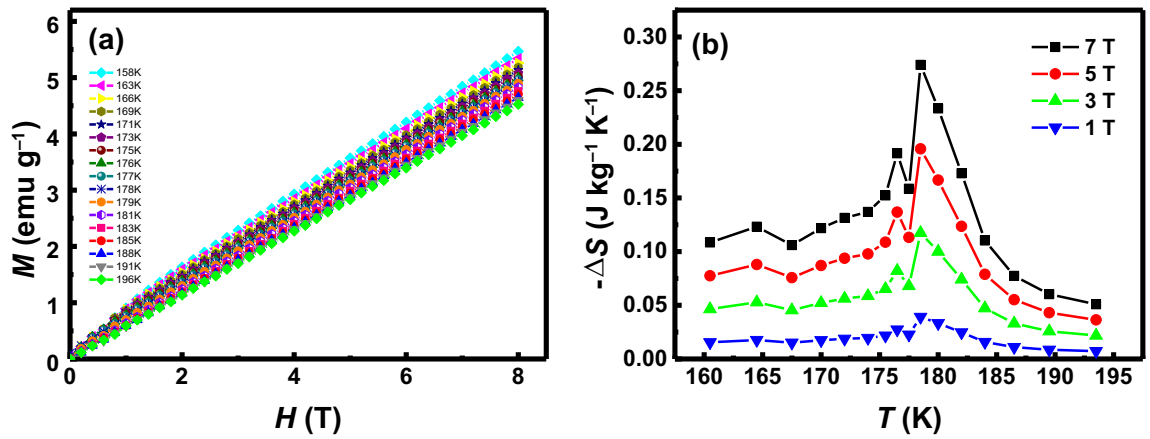

Figure 9. (**a**) Isothermal magnetization *vs.* applied magnetic field (*M–H* curves) in the first quadrant at different temperatures between 158 and 196 K. (**b**) Temperature-dependent magnetic entropy change (–ΔS) curves at different magnetic fields for the EDCO compounds.

Table 4. Magnetic entropy change (–-ΔS) and relative cooling power (RCP) at different applied magnetic fields.

H (T)	–-ΔS (J kg^{-1} K^{-1})	RCP (J kg^{-1})
1	0.03	0.58
3	0.11	1.76
5	0.19	2.94
7	0.27	4.27

Figure 9b displays the value of change in magnetic entropy (–ΔS) curves against the temperature (T) for several H values. It is noteworthy that the information about the magnetic transition can be obtained from the sign of –ΔS. For FM transition yields a positive value, while an AFM ordering exhibits a negative value because of an orientation disorder of the magnetic sublattices. Table 4 shows the obtained value of –ΔS at around the T_N with variation of various magnetic fields. The values are comparable with $YCrO_3$ and higher than that of the reported for $LaCrO_3$ and $SmCrO_3$ compounds under a 5 T applied magnetic field [6,59]. Relative cooling power (RCP) evaluates the efficiency of magnetic refrigeration, which is determined by the equation; $RCP = -\delta T_{FWHM} \times \Delta S$ [60].

The observed RCP values are listed in table 4 at different fields. The values of magnetic entropy change and RCP suggest that the present compound can be a suitable candidate for magnetic refrigeration.

4. Conclusions

In this study, polycrystalline $EuCrO_3$ and $Eu_{0.9}Dy_{0.10}CrO_3$ samples were synthesized via the conventional solid-state reaction method and their structural, optical and magnetic properties were studied in detail. XRD analysis revealed a single-phase orthorhombic perovskite structure with a *Pnma* space group for both compositions. FESEM images display the average grain sizes of approximately 300 ± 25 nm. Optical properties including the direct bandgap, skin depth (δ), extinction coefficient (k), refractive index (n) and optical conductivity (σ) are evaluated. DC magnetization measurements indicate a reduction in Néel temperature (T_N ~177 K) due to Dy substitution compared to the pristine $EuCrO_3$ (T_N ~181 K) compound. The hysteresis behaviour observed in the M–H loops is attributed to the presence of both FM and AFM components in the EDCO compound. Above T_N, the hysteresis loop disappears indicating paramagnetic behaviour. The magnetocaloric effect was assessed through magnetic entropy change (–ΔS) and RCP, with maximum values of –ΔS ~ 0.27 J kg^{-1} K^{-1} and RCP ~4.27 J kg^{-1} under 7 T applied field. These findings suggest that the EDCO compound can be appropriate for low-temperature magnetic refrigeration.

Acknowledgement

We would like to express our gratitude to the Central Instrumentation Facility, Central University of Rajasthan, Ajmer, for providing the physical property measurement system facility.

References

[1] Singh K D, Pandit R and Kumar R 2018 *Solid State Sci.* **85** 70
[2] Maity R, Dutta A, Halder S, Shannigrahi S, Mandal K and Sinha T P 2021 *Phys. Chem. Chem. Phys.* **23** 16060
[3] Su Y, Zhang J, Feng Z, Li L, Li B, Zhou Y *et al* 2010 *J. Appl. Phys.* **108** 013905
[4] Singh K D, Singh F, Choudhary R J and Kumar R 2020 *Appl. Phys. A Mater. Sci. Process.* **126** 1
[5] Li B, Tian F, Cui X, Xiang B, Zhao H, Zhang H *et al* 2022 *Nanomaterials* **12** 1773
[6] Fkhar L, Mahmoud A, Boschini F, Hamedoun M, Benyoussef A, Hlil E *et al* 2019 *J. Supercond. Nov. Magn.* **33** 15
[7] Prado-Gonjal J, Schmidt R, Romero J J, Ávila D, Amador U and Morán E 2013 *Inorg. Chem.* **52** 313
[8] Fabritchnyi P B, Afanasov M I, Mezhuev E M, Astashkin R A, Wattiaux A, Bordère S *et al* 2013 *Acad. Sci. Phys.* **77** 745
[9] Kumar S, Coondoo I, Vasundhara M, Puli V S and Panwar N 2017 *Phys. B Condens. Matter* **519** 69
[10] Yadav K, Kaur G, Sharma M K and Mukherjee K 2020 *Phys. Lett. Sect. A Gen. At. Solid State Phys.* **384** 126638
[11] Wang L, Wang S W, Zhang X, Zhang L L, Yao R and Rao G H 2016 *J. Alloys Compd.* **662** 268
[12] Yin S, Sharma V, McDannald A, Reboredo F A and Jain M 2016 *RSC Adv.* **6** 9475
[13] Shi J, Yin S, Seehra M S and Jain M 2018 *J. Appl. Phys.* **123** 0
[14] Franco V, Blázquez J S, Ipus J J, Law J Y, Moreno-Ramírez L M and Conde A 2018 *Mater. Sci.* **93** 112
[15] Moriya T 1960 *Phys. Rev.* **120** 91
[16] Aleonard R, Pauthenet R, Rebouillat J P and Veyret C 1978 *J. Appl. Phys.* **379** 4
[17] Mguedla R, Ben Jazia A, Saadi M, Khirouni K, Chniba-boudjada N and Boujelben W 2020 *J. Alloys Compd.* **812** 152130
[18] Mguedla R, Ben Jazia Kharrat A, Taktak O, Souissi H, Kammoun S, Khirouni K *et al* 2020 *Opt. Mater. (Amst).* **101** 109742
[19] Gupta P and Poddar P 2015 *RSC Adv.* **5** 10094
[20] Mguedla R, Ben Jazia Kharrat A, Kammoun S, Khirouni K and Boujelben W 2021 *Opt. Mater. (Amst).* **119** 111311
[21] Kanwar K, Coondoo I, Anas M, Malik V K, Kumar P, Kumar S *et al* 2021 *Ceram. Int.* **47** 7386
[22] Panwar N, Singh K, Kanwar K, Bitla Y, Kumar S and Puli V S 2022 *Crystals* **12** 15
[23] Yadav M and Rath C 2022 *J. Magn. Magn. Mater.* **543** 168610
[24] Sibanda E T, Prinsloo A R E, Sheppard C J and Mohanty P 2022 *AIP Adv.* **12** 035342

[25] Wang Q, Lv B, Wu Q, Hu X, Luo X, Fang J *et al* 2023 *Ceram. Int.* **49** 11903
[26] Kanwar K, Chen B R, Kuo Y K and Panwar N 2022 *Ceram. Int.* **49** 2506
[27] Siddique M N, Faizan M, Riyajuddin S, Tripathi P, Ahmad S and Ghosh K 2021 *J. Alloys Compd.* **850** 156748
[28] Yin S and Jain M 2016 *J. Appl. Phys.* **120** 043906
[29] Yin S, Sauyet T, Seehra M S and Jain M 2017 *J. Appl. Phys.* **121** 063902
[30] Ramírez J M M, Pessoni H V S, Franco A and Machado F L A 2017 *J. Alloys Compd.* **690** 315
[31] Taheri M, Kremer R K, Trudel S and Razavi F S 2015 *J. Appl. Phys.* **118** 124306
[32] Taheri M, Razavi F S, Yamani Z, Flacau R, Reuvekamp P G, Schulz A *et al* 2016 *Phys. Rev. B* **93** 1
[33] Prado-Gonjal J, Schmidt R, Ávila D, Amador U and Morán E 2012 *J. Eur. Ceram. Soc.* **32** 611
[34] Yin S, Seehra M S, Guild C J, Suib S L, Poudel N and Jain M 2017 *Phys. Rev. B* **95** 1
[35] Zhao Y, Weidner D J, Parise J B and Cox D E 1993 *Phys. Earth Planet. Inter.* **76** 1
[36] Patterson A L 1939 *Phys. Rev.* **56** 978
[37] Tripathi A K and Lal H B 1982 *J. Mater. Sci.* **17** 1595
[38] Jaiswal A, Das R, Adyanthaya S and Poddar P 2011 *J. Nanopart. Res.* **13** 1019
[39] Ullah R, Ali M A, Murtaza G, Mahmood A and Ramay S M 2021 *Mater. Sci. Semicond. Process.* **122** 105487
[40] Redinger A and Siebentritt S 2015 *Copp. Zinc Tin Sulfide-Based Thin-Film Sol. Cells* **627** 363
[41] Mott N F and Davis Davis E A 1970 *Philos. Mag.* **22** 903
[42] Siddique M N, Faizan M, Riyajuddin S, Tripathi P, Ahmad S and Ghosh K 2019 *J. Alloys Compd.* **850** 156748
[43] Mall A K and Pramanik A K 2020 *AIP Conf. Proc.* **2220** 3
[44] Panwar N, Coondoo I, Kumar S, Kumar S, Vasundhara M and Rao A 2019 *J. Alloys Compd.* **792** 1122
[45] Hassanien A S and Akl A A 2015 *J. Alloys Compd.* **648** 280
[46] Papavassiliou G C 1979 *Prog. Solid State Chem.* **12** 185
[47] Wemple S H and DiDomenico M 1971 *Phys. Rev. B* **3** 1338
[48] Hassanien A S and Sharma I 2020 *Optik (Stuttg).* **200** 163415
[49] Tounsi N, Barhoumi A, Chaffar Akkari F, Kanzari M, Guermazi H and Guermazi S 2015 *Vacuum* **121** 9
[50] Boudad L, Taibi M, Belayachi A and Abd-Lefdil M 2020 *J. Mater. Sci. Mater. Electron.* **31** 354
[51] Deng D, Wang X, Zheng J, Qian X, Yu D, Sun D *et al* 2015 *J. Magn. Magn. Mater.* **395** 283
[52] Durn A, Arvalo-Lpez A M, Castillo-Martnez E, Garca-Guaderrama M, Moran E, Cruz M P *et al* 2010 *J. Solid State Chem.* **183** 1863
[53] Yi K, Tang Q, Wu Z and Zhu X 2022 *Nanomaterials* **12** 1
[54] Dong Z, Wang Z and Yin S 2020 *Ceram. Int.* **46** 26632
[55] Patra K P and Ravi S 2022 *J. Magn. Magn. Mater.* **559** 169537
[56] Wu B, Guo D, Wang Y and Zhang Y 2020 *Ceram. Int.* **46** 11988
[57] Pecharsky V K and Gschneidner K A 1999 *J. Appl. Phys.* **86** 565
[58] Tishin A M 1998 *J. Magn. Magn. Mater.* **184** 62
[59] Oliveira G N P, MacHado P, Pires A L, Pereira A M, Araújo J P and Lopes A M L 2016 *J. Phys. Chem. Solids* **91** 182
[60] McDannald A and Jain M 2015 *J. Appl. Phys.* **118** 043904